PCCP

PAPER

View Article Online
View Journal | View Issue

Cite this: *Phys. Chem. Chem. Phys.*, 2014, **16**, 18294

The origin of high electrolyte–electrode interfacial resistances in lithium cells containing garnet type solid electrolytes†

Lei Cheng,*[ab] Ethan J. Crumlin,[c] Wei Chen,[a] Ruimin Qiao,[c] Huaming Hou,[ad] Simon Franz Lux,[a] Vassilia Zorba,[a] Richard Russo,[a] Robert Kostecki,[a] Zhi Liu,[c] Kristin Persson,[a] Wanli Yang,[c] Jordi Cabana,[ae] Thomas Richardson,[a] Guoying Chen[a] and Marca Doeff*[a]

Received 3rd July 2014,
Accepted 15th July 2014

DOI: 10.1039/c4cp02921f

www.rsc.org/pccp

Dense LLZO (Al-substituted $Li_7La_3Zr_2O_{12}$) pellets were processed in controlled atmospheres to investigate the relationships between the surface chemistry and interfacial behavior in lithium cells. Laser induced breakdown spectroscopy (LIBS), scanning electron microscopy (SEM), X-ray diffraction (XRD), Raman spectroscopy, synchrotron X-ray photoelectron spectroscopy (XPS) and soft X-ray absorption spectroscopy (XAS) studies revealed that Li_2CO_3 was formed on the surface when LLZO pellets were exposed to air. The distribution and thickness of the Li_2CO_3 layer were estimated by a combination of bulk and surface sensitive techniques with various probing depths. First-principles thermodynamic calculations confirmed that LLZO has an energetic preference to form Li_2CO_3 in air. Exposure to air and the subsequent formation of Li_2CO_3 at the LLZO surface is the source of the high interfacial impedances observed in cells with lithium electrodes. Surface polishing can effectively remove Li_2CO_3 and dramatically improve the interfacial properties. Polished samples in lithium cells had an area specific resistance (ASR) of only 109 Ω cm^2 for the LLZO/Li interface, the lowest reported value for Al-substituted LLZO. Galvanostatic cycling results obtained from lithium symmetrical cells also suggest that the quality of the LLZO/lithium interface has a significant impact on the device lifetime.

Introduction

Enabling durable cycling of metal anodes, especially lithium, is a critical step toward breakthroughs in battery performance that surpass current Li-ion technologies, especially if coupled with high storage capacity cathode couples such as sulfur or oxygen.[1–3] However, safety concerns, due to the dendritic growth of lithium during cycling with conventional liquid electrolytes, present formidable obstacles to development. Solid ceramic electrolytes have been proposed as a solution to this problem, provided that the criteria of high ionic conductivity and good chemical stability with metallic lithium can be met. An ionic conductivity of at least 10^{-3} to 10^{-4} S cm^{-1} is required to achieve comparable transport properties to liquid electrolytes for practical use.[4] Several highly conductive materials such as $Li_{1+x}Al_xTi_{2-x}(PO_4)_3$ (LATP)[5] and $Li_xLa_{2/3-x}TiO_3$(LLTO)[6] with bulk ionic conductivities in the range of 10^{-3} S cm^{-1} are, however, unstable against lithium anodes.[7] Other chemically stable materials (LiPON[8] and $Li_{3.4}Si_{0.4}P_{0.6}O_4$[9,10]) are not sufficiently conductive at room temperature to be practical in most devices. Other highly conductive phases such as $Li_{10}GeP_2S_{12}$ (LGPS)[11] that do not contain oxygen have also drawn a lot of research interest recently, but their instability against reduction by lithium and exposure to moisture make them difficult to use.[12] Given these considerations, highly conductive ($\sigma \cong 4 \times 10^{-4}$ S cm^{-1}) cubic garnet phases based on $Li_7La_3Zr_2O_{12}$ (LLZO) are presently the most promising.[13–16] However, the application of LLZO in lithium metal batteries is hindered by high interfacial resistance at the lithium metal anode side. In general, the high interfacial resistance between the solid ceramic electrolyte and metallic lithium dominates the cell behavior, limiting the device to low current density cycling.[17,18] An area specific

[a] *Lawrence Berkeley National Laboratory, Environmental Energy Technologies Division, University of California, One Cyclotron Road, Bldg 62, Berkeley, CA 94720, USA. E-mail: leicheng@lbl.gov, mmdoeff@lbl.gov*
[b] *Department of Material Sciences and Engineering, University of California, Berkeley, CA 94720, USA*
[c] *Advanced Light Source, Lawrence Berkeley National Laboratory, University of California, Berkeley, CA 94720, USA*
[d] *Optics and Optoelectronics Laboratory, Ocean University of China, Qingdao 266100, China*
[e] *Department of Chemistry, University of Illinois at Chicago, Chicago, IL 60607, USA*

† Electronic supplementary information (ESI) available. See DOI: 10.1039/c4cp02921f

resistance (ASR) smaller than 100 Ω cm^2 is required for the LLZO/Li interface to ensure that the voltage drops no more than 100 mV, at a current density of 1 mA cm^{-2}.[19]

Poor electrode/electrolyte contact, slow charge transfer, and sluggish carrier transport in the interfacial region all can increase interfacial resistance. Buschmann *et al.*[20] reported an ASR of 2800 Ω cm^2 for cells containing LLZO doped with 0.9 wt% Al, and an ASR close to 6000 Ω cm^2 was observed for a Ga-doped LLZO/Li interface.[21] Attempts to decrease interfacial resistance by applying high external pressure to improve physical contact have been partially successful for some systems: Liang's group reported low interfacial resistance (100–200 Ω cm^2) by directly compacting either a Li_3PS_4 solid electrolyte or a LLZO–Li_3PS_4 composite electrolyte powder onto soft lithium foil under 300 MPa pressure.[22,23] The decrease in interfacial resistance was attributable to the large effective contacting area and good physical adhesion. Low interfacial resistances have also been achieved by pressing lithium foil onto densified Nb and Ta substituted LLZO under 150 MPa pressure.[24,25] Another proposed strategy to lower interfacial resistance has been to tune the chemical composition of LLZO. Early work by Thangadurai and Weppner showed that the garnet-type $Li_6ALa_2Ta_2O_{12}$ (A = Sr, Ba) had minimal electrolyte–electrode interfacial resistance in lithium cells.[26] However, these phases are less promising than LLZO given their much lower room temperature conductivities of 10^{-6}–10^{-5} S cm^{-1}. Buschmann *et al.* demonstrated that LLZO co-substituted by optimal amounts of Ta and Al can achieve an order of magnitude lower interfacial resistance than the Al substituted counterparts.[27] Recently, Cheng *et al.* reported an ASR of 540 Ω cm^2 for an Al-substituted LLZO synthesized with a stoichiometric amount of Li_2CO_3, rather than an excess.[28] This value, which is lower than that found in the earlier reports, suggests that the Li_2CO_3 content critically affects the ASR.

In this work, we investigated the effect of post-processing conditions on the LLZO pellets and the relationship between surface properties and electrochemical performance. We report that the high interfacial resistance primarily originates from LLZO instability in air; a surface insulating layer is formed upon exposure to the ambient environment. A good LLZO/Li interface with low resistance can be achieved through a simple polishing procedure, removing one obstacle and bringing this material a substantial step closer to practical utilization in high energy cells.

Experimental

Al-substituted LLZO powders and pellets were prepared using the same procedures outlined in our previous work.[28] The surfaces of sintered pellets were polished in ambient air or in an Ar glove box, using several pieces of polishing papers with grit numbers progressing from 320–600 so that an approximately 50 μm thick layer was removed from each surface. Samples polished in air were stored in the ambient environment for periods of several days to weeks, while those polished under Ar were stored in the glove box for similar periods of time. Specifically, the LLZO_air sample used for the LIBS experiment had been aged in air for a period of about two months, whereas samples used for spectroscopic and electrochemical experiments had been exposed for several days.

Sintered pellets were characterized by X-ray powder diffraction (XRD) using a Bruker D2-Phaser with CuKα radiation (λ = 1.54178 Å). The pure cubic LLZO pattern was simulated using PowderCell 2.4 (W. Kraus and G. Nolze, Federal Institute for Materials Research and Testing, Rudower Chaussee 5, 12489 Berlin, Germany) and unit cell parameters taken from ref. 16. Images of pellet surface morphologies were obtained by scanning electron microscopy (SEM) using a JEOL-7500F field emission microscope. Chemical composition analyses were performed using inductively coupled plasma optical emission spectrometer (ICP-OES). As sintered pellets were polished and sent to Evans Analytical Group for elemental analyses.

Confocal Raman microscopy was performed using a WITec alpha300 S confocal microscope coupled to a Raman spectrometer (1800 grooves per mm grating) equipped with a CCD detector (UHTS-300). A fiber-coupled laser operating at 532 nm was used to stimulate Raman scattering. The laser power applied to the sample was approximately 30 mW. Excitation laser light was focused onto the sample using a Nikon E Plan objective lens with 20× magnification and NA = 0.4. Light from the sample was collected using the same lens and passed through a fluorescence filter to the remove non-scattered and Rayleigh-scattered laser light and then focused on to a pinhole at the entrance of an optical fiber that leads to the spectrometer. Spectra were collected using a single five-second integration.

Femtrosceond laser induced breakdown spectroscopy (LIBS) was used to image the cross-sectional elemental distributions in a pellet polished in ambient air (LLZO_air). The experimental setup, data processing and image reconstruction are described in detail in our previous work.[28] Briefly, a femtosecond laser at 343 nm served as an excitation source. The LIBS atomic lines of Li and Zr at 460.3 nm and 468.8 nm were detected using an optical spectrometer/ICCD system and were subsequently analyzed. Spatially-resolved 2D cross-sectional imaging was achieved by scanning the sample in 2 axes (lateral and axial) with respect to the femtosecond laser beam, followed by chemical map reconstruction.

X-ray photoelectron spectroscopy (XPS) was carried out at bending magnet beamline 9.3.2 at the Advanced Light Source (ALS) at the Lawrence Berkeley National Laboratory (LBNL). XPS data of Li 1s, C 1s, O 1s, Zr 3d and La 4d were collected at 640 eV from the top surface of LLZO samples in ultrahigh vacuum with a sampling size 1 mm in diameter. Binding energy correction of spectra was done by calibration to the C 1s photoemission peak of adventitious hydrocarbons at 285 eV. Soft X-ray absorption spectroscopy (XAS) measurements of C and O K-edges were performed at undulator beamline 8.0.1 at the ALS at LBNL, where the intense photon beam from a spherical grating monochromator gives an energy resolution better than 0.2 eV. Experiments were performed at ambient temperature. Data were collected in both surface-sensitive total electron yield (TEY) and bulk-sensitive total fluorescence yield

(TFY) modes. All the spectra have been normalized to the beam flux measured by the upstream gold mesh. The same sample sets were used for XPS and XAS measurements. Samples were protected in an Ar environment during transfer.

AC impedance measurements were obtained on dense pellets using a VMP3 multichannel potentiostat/galvanostat (Bio-Logic Science Instruments). For the experiments with blocking electrodes, a gold layer was sputtered on both sides of the pellet and Pt meshes and wires were attached and used as current collectors. For cells with non-blocking electrodes, soft metallic lithium was first spread on both sides of the dense pellet. Afterwards, the pellet was sandwiched between lithium foil disks in a Swagelok-type cell. Measurements were made at frequencies from 1 MHz to 1 Hz. Impedances were determined from the intercepts of the relevant capacitive arcs at the real axes in the Nyquist plots and conductivities calculated using the equation $\sigma = (1/Z)(L/A)$, where Z is the impedance, L is the pellet thickness, and A is the pellet area. Typical dimensions of the pellets were around 1.1 mm thick and 7.8 mm in diameter. Activation energies were determined from the behavior of the conductivity as a function of temperature using the Arrhenius equation. Cells were cycled at ambient temperature inside an Ar-filled glove box at a constant current density of 46 μA cm^{-2}. For the moisture experiment, pellets first polished in the Ar glove box and assembled into cells with lithium electrodes for AC impedance measurements were removed from the cell holder, and electrodes were peeled off. Residual lithium adhering to the surfaces was quickly washed away with de-ionized water in air. The pellet was dried and then transferred back in an Ar glovebox and re-assembled into a cell with lithium electrodes for further impedance analysis.

Results and discussion

As-sintered pellets were 92% dense (theoretical density = 5.1 g cm^{-3}), and had grain sizes between 150–200 μm. Several sintered pellets were polished in an Ar glovebox with oxygen levels below 0.1 ppm (designated LLZO_Ar) and others in air as a control experiment (designated LLZO_air). LLZO_Ar was stored in the Ar glovebox while LLZO_air was stored in air. Fig. 1 shows the top-view scanning electron microscope (SEM) images of unpolished LLZO, LLZO_air and LLZO_Ar pellets. The polished surfaces of LLZO_air and LLZO_Ar had similar morphologies, ruling out the effect of different contact areas on the interface impedance.

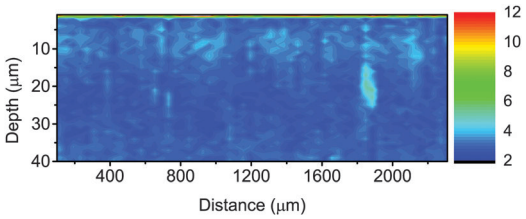

Fig. 2 2-D cross-section of the Li/Zr atomic ratio in the LLZO_air pellet, aged in air for about two months, obtained by LIBS.

Fig. 2 shows the laser-induced breakdown spectroscopic (LIBS) cross section mapping of an LLZO_air sample, which had been aged in air for about two months. The atomic ratio of Li/Zr was mapped out as functions of the lateral distance and vertical depth with resolutions of 38 μm and 1 μm, respectively. The chemical map shows that a Li-rich region was present on the pellet surface suggesting an impurity formed due to chemical instability in the ambient environment. Due to the limitations of the experiment, it was not possible to determine the chemical identity of this lithium-rich phase or the exact thickness of the layer. However, the observation is in agreement with the report by Shimonishi *et al.* on increased grain-boundary resistance after immersion of LLZO in water at 50 °C,[29] and that of Larraz *et al.* suggesting that the LLZO cubic structure is very sensitive to ambient conditions, especially moisture.[30] Additionally Jin *et al.* found that LLZO reacts with water with possible formation of LiOH.[31] (LiOH reacts with CO_2 to from Li_2CO_3 in air)[32] Thus, we speculate that the high Li/Zr intensity layer is composed of LiOH and Li_2CO_3, resulting from the chemical instability of LLZO against moisture and from exposure to CO_2.

X-ray diffraction (XRD) and Raman spectroscopy were then used to obtain further information about the high lithium intensity layer on the pellet surface (Fig. S1, ESI†). No apparent differences were observed between LLZO_Ar and LLZO_air in the XRD and Raman spectra, implying that the high Li intensity surface layer was so thin that it was below the sensitivity limits of these techniques. Thus, surface sensitive techniques with varying probing depths, such as synchrotron X-ray photoelectron spectroscopy (XPS)[33] and soft X-ray absorption spectroscopy (sXAS),[34] are necessary to identify the surface chemical species, particularly for samples exposed to air for short periods of time.

XPS was used to compare the surface chemistry of LLZO polished in air and exposed for several days to the ambient

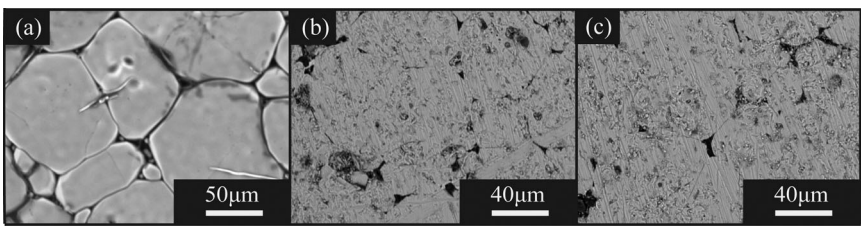

Fig. 1 SEM surface morphologies of (a) an as-sintered LLZO pellet (b) a LLZO pellet polished in an Ar glovebox (LLZO_Ar) and (c) a LLZO pellet polished in air (LLZO_air) and exposed to the ambient atmosphere for several days.

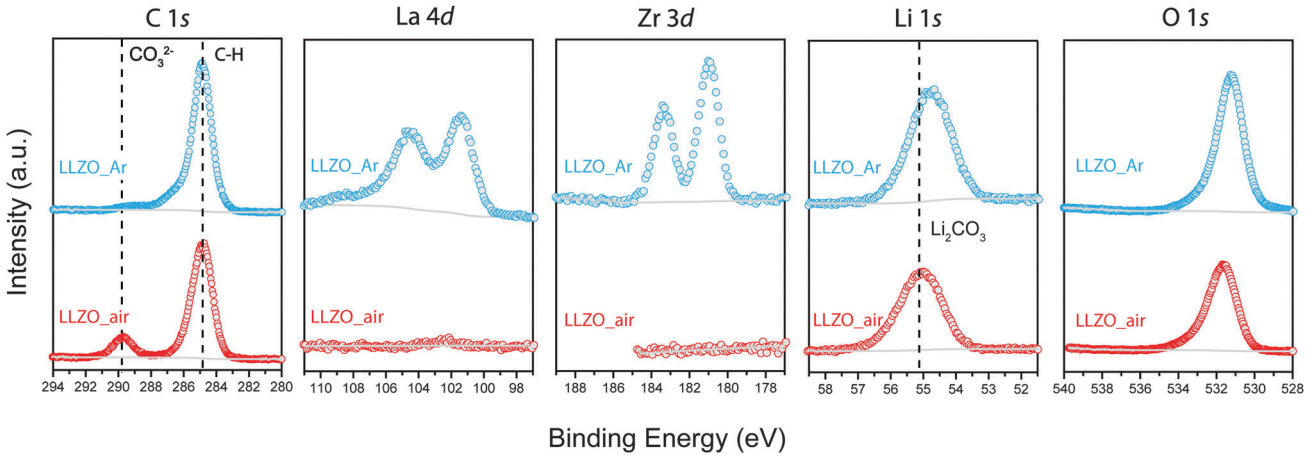

Fig. 3 C 1s, La 4d, Zr 3d and Li 1s XPS data collected from LLZO Ar and LLZO_air pellet surfaces under ultra-high vacuum.

atmosphere, and the one polished in Ar.[35] The C 1s, La 4d, Zr 3d, Li 1s, and O 1s spectra collected at 640 eV for the LLZO_air and LLZO_Ar samples (Fig. 3) provided concrete evidence of Li_2CO_3 on the surfaces of the former. Two peaks were identified at binding energies of 285.0 eV and 290.0 eV in the C 1s spectra of LLZO_air; the first is due to adventitious carbon, and the one at 290.0 eV is assigned to carbonate based on previously reported C 1s spectra of Li_2CO_3.[36] In contrast, the carbonate peak was not observed in the LLZO_Ar C 1s spectra. Other differences included the presence of La 4d and Zr 3d doublets in the spectra of LLZO_Ar pellets, which were not observed in LLZO_air. They provide evidence that air exposure led to the formation of a surface carbonate layer on the LLZO-air pellets thick enough to block the La and Zr photoelectron signals. This analysis was further substantiated by the Li 1s XPS spectra. The Li 1s peak for LLZO_air shifted to a higher binding energy close to 55.3 eV, similar to the reported binding energy of Li_2CO_3. The lower binding energy of 54.5 eV observed for the LLZO_Ar sample is tentatively attributed to Li in LLZO, with the shift explained by the weaker Li–O bond in LLZO. Similarly, the LLZO_air O 1s spectra showed a binding energy shift relative to that of LLZO_Ar, consistent with the oxygen belonging to Li_2CO_3 on the pellet surfaces. In general, the inelastic mean free path (IMFP) of electrons in the energy range of 50–600 eV is between 0.6–1.5 nm in inorganic materials.[37] The probing depth (taken as 3 times the IMFP) is between 1.8–4.5 nm for these experiments. Since all Zr 3d and La 4d signals were attenuated by the Li_2CO_3 layer, the lower bound for the thickness estimation of the Li_2CO_3-containing layer is *ca.* 3 nm.

Soft XAS was then employed to estimate the upper bound of the thickness of the Li_2CO_3 and to extend the understanding of LLZO surface chemistry on the same samples studied by XPS. We utilized both surface-sensitive total electron yields (TEY, probing depth <10 nm) and bulk-sensitive total fluorescence yields (TFY probing depth >100 nm) modes to obtain depth-dependent chemical information.[38,39] Fig. 4(a) shows the normalized O K-edge TEY spectra of the LLZO_air, LLZO_Ar pellets, and a Li_2CO_3 reference. The pure Li_2CO_3 spectrum (top) exhibited a peak at 534.1 eV, which was assigned to electron transition from the O-1s to π* (C═O) orbital. The leading edge in the LLZO_Ar TEY spectrum appeared at a lower photon energy of 533.0 eV, which is associated with the oxygen of LLZO, and no

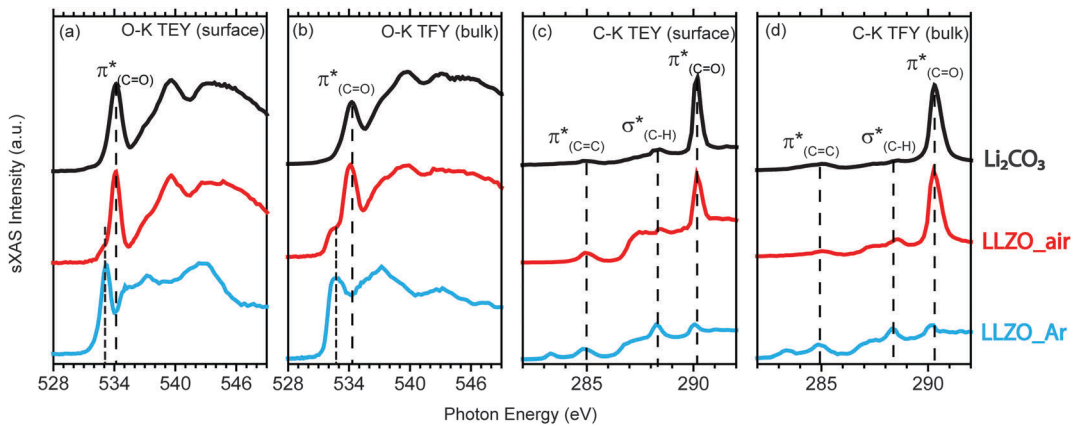

Fig. 4 (a) and (b) O K-edge XAS spectra of LLZO_Ar, LLZO_air and the Li_2CO_3 reference collected in TEY and TFY modes; (c) and (d) C K-edge XAS spectra of LLZO_Ar, LLZO_air and the Li_2CO_3 reference collected in TEY and TFY modes.

Li_2CO_3 signal was detected. The TEY spectrum of LLZO_air (middle) resembled that of the pure Li_2CO_3 reference. These observations confirmed the XPS finding that Li_2CO_3 was found on the surfaces of the LLZO_air pellets but not on those of LLZO_Ar. Both the bulk-sensitive TFY spectra of the LLZO_air and the LLZO_Ar samples showed LLZO peaks at 533.0 eV. An additional O-K absorption feature at 534.1 eV was observed for the former due to the Li_2CO_3 layer on the pellet surface (Fig. 4(b) middle and bottom). The strong LLZO feature at 533.0 eV is a clear indication that the thickness of the Li_2CO_3 layer on the LLZO_air pellet is below the ~100 nm detection depth of the TFY mode. In addition, the appearance of a weak peak at 533.0 eV in the LLZO_air TEY spectrum (Fig. 4(a) middle) implies that the Li_2CO_3 thickness is close to or slightly lower than the 10 nm detection depth of the TEY mode.

Further insight was obtained from the C K-edge XAS spectra. Fig. 4(c) and (d) are plots of the C K-edge XAS spectra collected in TEY and TFY mode, respectively. There are three absorption features at 285.0 eV, 288.1 eV and 290.1 eV in the spectrum of the Li_2CO_3 reference (Fig. 4(c) and (d) top). The first two features are assigned to adventitious carbon. The feature at 290.1 eV is attributable to the transition from the C 1s to π* (C═O) orbital of Li_2CO_3. In both the TEY and TFY data, the LLZO_air spectra are very similar to the Li_2CO_3 reference in accordance with the LIBS, XPS, and O-K XAS results and confirm the presence of Li_2CO_3 on the pellet surface. In contrast, the LLZO_Ar sample showed a much weaker C-K absorption intensity at 290.1 eV, indicating the presence of a trace amount of Li_2CO_3. An additional weak absorption feature observed at 283.0 eV in both the LLZO_Ar TEY and TFY spectra are possibly the result of contamination with a carbon-containing impurity during polishing in the Ar glove box.

To better understand the Li_2CO_3 formation on the LLZO pellet during air exposure, we calculated first-principles energies to estimate the Gibbs free reaction energy at standard states for relevant reactions.[40,41] One unit cell of $Li_{56}La_{24}Zr_{16}O_{96}$ was considered to save computational cost (Fig. S2, ESI†). Formation of Li_2CO_3 is accompanied by loss of Li in LLZO, which is likely to be associated with concurrent O loss to balance the charge, resulting in $Li_{54}La_{24}Zr_{16}O_{95}$. The loss of lithium was supported experimentally by elemental analysis using inductively coupled plasma atomic emission spectroscopy (ICP-OES).[28] Further loss of lithium and oxygen may result in decomposition of the LLZO cubic phase to $La_2Zr_2O_7$, as observed by Huang *et al.*[42] We assume that this process is unlikely for samples exposed briefly to air. Gibbs free energies of all the related chemical species are tabulated in Table S1 (ESI†). The Gibbs free energy for reaction (1) of LLZO with gas phase H_2O to form Li deficient $Li_{54}La_{24}Zr_{16}O_{95}$ and LiOH was −0.55 eV fu^{-1}. LiOH then absorbs CO_2 from air, forming Li_2CO_3.[43] In addition, we also found an energetic preference for reaction (2) in which LLZO reacts directly with CO_2 without participation from water to form Li_2CO_3. The Gibbs free energy for this reaction is −2.00 eV fu^{-1}, indicating that LLZO is thermodynamically unstable against the reaction with dry CO_2 as well. Thus, there is a thermodynamic preference for LLZO to form Li_2CO_3 upon exposure to air, consistent with the experimental observations. The kinetics of these reactions require further experimentation to determine. Time-dependent spectroscopic investigations are currently underway in our laboratory to obtain these details.

$$Li_{56}La_{24}Zr_{16}O_{96}(s) + H_2O(g) = Li_{54}La_{24}Zr_{16}O_{95}(s) + 2LiOH(s) \quad (1)$$

$$Li_{56}La_{24}Zr_{16}O_{96}(s) + CO_2(g) = Li_{54}La_{24}Zr_{16}O_{95}(s) + Li_2CO_3(s) \quad (2)$$

Ionic conductivity measurements using AC impedance with Au blocking electrodes showed minimal differences between the total conductivities of LLZO_air exposed to the ambient environment for several days and LLZO_Ar pellets (Fig. S3, ESI†). This is consistent with the XPS and XAS observations that the Li_2CO_3 layer was thin and did not affect the bulk properties. In contrast, electrochemical impedance spectroscopy (EIS) measurements using non-blocking Li metal electrodes with LLZO pellets sandwiched in between in a symmetric cell configuration revealed large differences in the interfacial resistances. Both LLZO_air and LLZO_Ar cells showed one partial semicircle in the high frequency range and a complete semicircle at lower frequencies in the Nyquist plots (Fig. 5). The semicircles at high frequencies are attributable to the total resistance of the LLZO pellets by comparison to the data obtained in cells with blocking electrodes, and the low frequency semi-circles can be assigned to the interfacial resistance.[9,28] An $(R_{pellet}Q_{pellet})(R_{interface}Q_{interface})$ equivalent circuit (see inset of Fig. 5) was used to fit the EIS data, where Q represents a constant phase element (CPE). Total resistances and capacitances of the pellets and interfaces were determined from the fit and are tabulated in Table 1. Area specific resistances (ASRs) of the interfaces were estimated by normalization to the pellet areas (0.45 cm^2). The interfacial resistance for the cell made with LLZO_air was 960 Ω cm^2. This value is similar to that of freshly sintered, unpolished LLZO pellets previously reported by us.[28] Note that the variation in interfacial resistance is probably attributable to the fact that the surface roughnesses of the polished LLZO_air and unpolished sintered pellet differ.

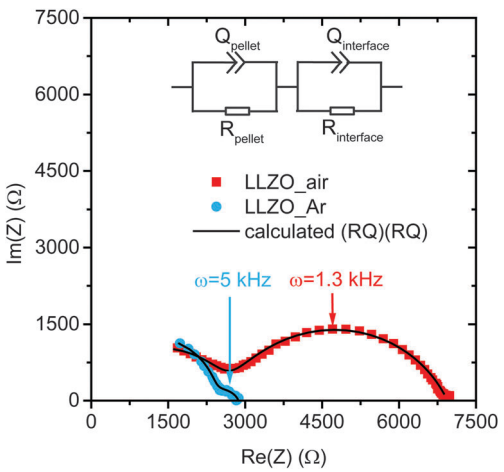

Fig. 5 Nyquist plots of symmetrical cells containing pellets sandwiched between lithium electrodes. (Figure inset: $(R_{pellet}Q_{pellet})(R_{interface}Q_{interface})$ equivalent circuit).

Table 1 Fitted resistances and capacitances of pellets and interfaces in Li/LLZO/Li cells with lithium electrodes, using an $(R_{pellet}Q_{pellet})(R_{interface}Q_{interface})$ equivalent circuit. Area specific resistances (ASR) of interfaces are also provided (note the interfacial resistance includes contributions from two identical LLZO/Li interfaces); these values have been divided in half to obtain the ASR of a single interface

Item	Pellet resistance (Ω)	Pellet capacitance (nF)	Interfacial resistance (Ω)	Interfacial capacitance (μF)	ASR (Ω cm^2)
LLZO_air	2652	1.82	4307	0.30	960
LLZO Ar	2355	0.85	491	0.72	109

The interfacial resistance of LLZO_Ar was 109 Ω cm^2, almost an order of magnitude lower than that of LLZO_air. This strongly suggests that the thin Li_2CO_3 layers on the pellet surfaces of the latter are responsible for the high interfacial resistance.

To further confirm that the high interfacial impedance could be due to the reaction of LLZO surfaces with moisture and CO_2, impedance experiments were performed on a cell containing an LLZO_Ar sample exposed to air and water after the initial measurements shown in Fig. S4 (ESI†) were obtained (see the Experimental section). The interfacial resistance increased greatly in magnitude after exposure, whereas the total conductivity was unaffected (Fig. S4, ESI†).

The temperature dependence of the reciprocal ASR followed a classical Arrhenius behavior with an activation energy of 0.33 eV, as shown in Fig. S5(a) (ESI†), indicating a stable electrolyte–electrode interface upon heating.[9] This value was close to the activation energy of the LLZO pellet total ionic conductivity as observed by other groups.[17,27] EIS measurements on symmetric lithium cells with LLZO_Ar samples using biases of 0 mV, 50 mV, 100 mV, 200 mV and 500 mV and 25 mV perturbations revealed that the interfacial resistance has no bias dependence (Fig. S5(b), ESI†), indicating that charge transfer was not the limiting step for interfacial resistance.

The Li/LLZO/Li symmetric cells were galvanostatically cycled. The behavior was also greatly improved when LLZO_Ar was used as an electrolyte, compared to that using LLZO_air (Fig. 6). An LLZO_air cell cycled at a current density of 46 μA cm^{-2} showed large and increasing overpotentials, above 100 mV. In contrast, LLZO_Ar was stable at 35 mV when the same current density was applied. The DC resistance calculated for both cells agreed well with the EIS measurements, and confirmed that the high ASR observed in the cell with the LLZO_air sample was a major contributor to the high observed overpotential. The difference in ASRs for the two cells also affected the cycling behavior; the cell containing LLZO_Ar cycled stably for the ten hours of the test, whereas the one with LLZO_air shorted in less than one hour. Thus, the quality of the electrode electrolyte interface is also a critical factor in determining the cell lifetime.

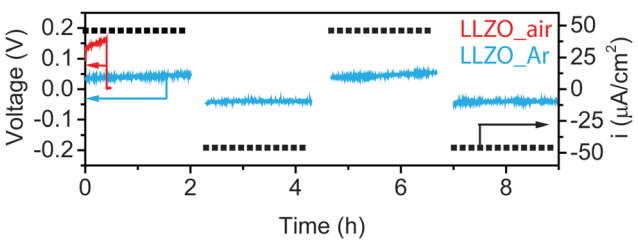

Fig. 6 Galvanostatic cycling of symmetrical cells with lithium electrodes and LLZO at a current density of 46 μA cm^{-2}.

Conclusions

We showed both experimentally and theoretically that Li_2CO_3 forms as a result of LLZO exposure to air. A combination of surface sensitive characterization techniques allowed an estimate to be made for the Li_2CO_3 layer thickness of between 3–100 nm thick for samples exposed to air for several days, but probably closer to about 10 nm. Exposure to air and the resulting formation of Li_2CO_3 are the origins of the large interfacial resistances observed in LLZO symmetric cells with lithium metal electrodes. The surface Li_2CO_3 can be easily removed by polishing pellets under an Ar atmosphere. When applied to the samples used in this study, this procedure resulted in the lowest interfacial impedance for Al substituted LLZO cells reported to date, and resulted in much more stable galvanostatic cycling than with the unprocessed material. While the chemical instability of LLZO towards moisture and air complicates the processing of the material into thin films needed for electrochemical cells, these results show that high interfacial impedances are not intrinsic to the system, but can be avoided with simple precautions.

Acknowledgements

We would like to thank Dr Jason Forster and Dr Jeffrey Urban from the Molecular Foundry at Lawrence Berkeley National Laboratory for assistance in recording the Raman spectra. Work at the Molecular Foundry was supported by the Office of Science, Office of Basic Energy Sciences, of the U.S. Department of Energy under Contract No. DE-AC02-05CH11231. The Materials Project Center (BES DOE Grant No. EDCBEE.) is gratefully acknowledged for funding, data and algorithmic support. LC acknowledges Prof. Werner Weppner for the discussion of garnet-type lithium super ionic conductors at the 224th ECS meeting, San Francisco, 2013. This work was supported by the Assistant Secretary for Energy Efficiency and Renewable Energy, Office of Vehicle Technologies and the Chemical Sciences, Geosciences, and Biosciences Division, Office of Basic Energy Sciences of the U.S. Department of Energy under contract no. DE-AC02-05CH11231. The Advanced Light Source is supported by the Director Office of Science, Office of Basic Energy Sciences, of the U.S. Department of Energy under Contract No. DE-AC02-05CH11231. The work of VZ was supported by the U.S. Department of Energy, Small Business Innovation Research Programs Office through Applied

References

1 G. Girishkumar, B. McCloskey, A. C. Luntz, S. Swanson and W. Wilcke, *J. Phys. Chem. Lett.*, 2010, **1**, 2193.
2 X. Ji, K. T. Lee and L. F. Nazar, *Nat. Mater.*, 2009, **8**, 500.
3 K. Gallagher, S. Goebel, T. Greszler, M. Mathias, W. Oelerich, D. Eroglu and V. Srinvasan, *Energy Environ. Sci.*, 2014, **7**, 1555.
4 K. Takada, *Acta Mater.*, 2013, **61**, 759.
5 J. Aono, E. Sugimoto, Y. Sadaoka, N. Imanaka and G. Adachi, *Solid State Ionics*, 1991, **47**, 257.
6 A. Belous, G. Novitskaya, S. Polyaneskaya and Y. Gornikov, *Izv. Akad. Nauk SSSR*, 1987, **23**, 470.
7 P. Knauth, *Solid State Ionics*, 2009, **180**, 911.
8 J. Bates, N. Dudney, G. Gruzalski, R. Zuhr, A. Choundhury, F. Luck and J. Robertson, *Solid State Ionics*, 1992, **53**, 647.
9 Y. Hu, D. Raistrick and R. Huggins, *J. Electrochem. Soc.*, 1977, **124**, 1240.
10 L. Zhang, L. Cheng, J. Cabana, G. Chen, M. M. Doeff and T. J. Richardson, *Solid State Ionics*, 2013, **231**, 109.
11 N. Kamaya, K. Homma, Y. Yamakawa, M. Hirayama, R. Kanno and M. Yonemura, *Nat. Mater.*, 2011, **10**, 628.
12 S. Ong, Y. Mo, W. Richards, L. Miara, H. S. Lee and G. Ceder, *Energy Environ. Sci.*, 2013, **6**, 148.
13 R. Murugan, V. Thangadurai and W. Weppner, *Angew. Chem.*, 2007, **119**, 7925.
14 M. Kotobuki, K. Kanamura, Y. Sato and T. Yoshida, *J. Power Sources*, 2011, **196**, 7750.
15 J. Park, L. Cheng, V. Zorba, A. Mehta, J. Cabana, G. Chen, M. Doeff, T. Richardson, J. Park, J. Son and W. Hong, *Thin Solid Films*, 2014, submitted.
16 C. A. Geiger, E. Alekseev, B. Lazic, M. Fish, T. Armbruster, R. Langner, M. Fechtelkord, N. Kim, T. Pettke and W. Weppner, *Inorg. Chem.*, 2011, **50**, 1089.
17 S. Ohta, T. Kobayashi, J. Seki and T. Asaoka, *J. Power Sources*, 2012, **202**, 332.
18 S. Ohta, S. Komagata, J. Seki, T. Saeki, S. Morishita and T. Asaoka, *J. Power Sources*, 2013, **238**, 53.
19 J. Christensen, P. Albertus, R. Sanchez-Carrera, T. Lohmann, B. Kozinsky, R. Liedtke, J. Ahmed and A. Kojic, *J. Electrochem. Soc.*, 2012, **159**, R1.
20 H. Buschmann, J. Dolle, S. Berendts, A. Kuhn, P. Bottke, M. Wilkening, P. Heitjans, A. Senyshyn, H. Ehrenberg, A. Lotnyk, V. Duppel, L. Kienle and J. Janek, *Phys. Chem. Chem. Phys.*, 2011, **13**, 19378.
21 H. E. Shinawi and J. Janek, *J. Power Sources*, 2013, **225**, 13.
22 E. Rangasamy, G. Sahu, J. Keum, A. Rondinone, N. Dudney and C. Liang, *J. Mater. Chem. A*, 2014, **2**, 4111.
23 Z. Liu, W. Fu, A. Payzant, X. Yu, Z. Wu, N. Dudney, J. Kiggans, K. Hong, A. Rondinone and C. Liang, *J. Am. Chem. Soc.*, 2013, **135**, 975.
24 K. Ishiguro, Y. Nakata, M. Matsui, I. Uechi, Y. Takeda, O. Yamamoto and N. Imanishi, *J. Electrochem. Soc.*, 2013, **160**, A1690.
25 K. Ishiguruo, H. Nemori, S. Sunahiro, Y. Nakata, R. Sudo, M. Matsui, Y. Takeda, O. Yamamoto and N. Imanishi, *J. Electrochem. Soc.*, 2014, **161**, A668.
26 V. Thangadurai and W. Weppner, *Adv. Funct. Mater.*, 2005, **15**, 107.
27 H. Buschmann, S. Berendts, B. Mogwitz and J. Janek, *J. Power Sources*, 2012, **206**, 236.
28 L. Cheng, J. S. Park, H. Hou, V. Zorba, G. Chen, T. Richardson, J. Cabana, R. Russo and M. Doeff, *J. Mater. Chem. A*, 2014, **2**, 172.
29 Y. Shimonishi, A. Toda, T. Zhang, A. Hirano, N. Imanishi, O. Yamamoto and Y. Takeda, *Solid State Ionics*, 2011, **183**, 48.
30 G. Larraz, A. Orera and M. L. Sanjuan, *J. Mater. Chem. A*, 2013, **1**, 11419.
31 Y. Jin and P. McGinn, *J. Power Sources*, 2013, **239**, 326.
32 D. Williams and R. Miller, *Ind. Eng. Chem. Fundam.*, 1970, **9**, 457.
33 M. Grass, P. Karlsson, F. Aksoy, M. Lundqvist, B. Wannberg, B. Mun, Z. Hussain and Z. Liu, *Rev. Sci. Instrum.*, 2010, **81**, 053106.
34 W. Yang, X. Liu, R. Qiao, P. Olalde-Velasco, J. Spear, L. Roseguo, J. Pepper, Y. Chuang, J. Denlinger and Z. Hussain, *J. Electron. Spectrosc. Relat. Phenom.*, 2013, **190**, 64.
35 Y. Lu, E. Crumlin, G. Veith, J. Harding, E. Mutoro, L. Baggetto, N. Dudney, Z. Liu and Y. Shao-Horn, *Sci. Rep.*, 2012, **2**, 715.
36 K. P. C. Yao, D. Kwabi, R. Quinlan, A. Mansour, A. Grimaud, Y. Lee, Y. Lu and Y. Horn, *J. Electrochem. Soc.*, 2013, **160**, A824.
37 S. Tanuma, C. Powell and D. Penn, *Surf. Interface Anal.*, 1991, **17**, 927.
38 R. Qiao, Y. Chuang, S. Yan and W. Yang, *PLoS One*, 2012, **7**, 11.
39 R. Qiao, I. Lucas, A. Karim, J. Syzdek, X. Liu, W. Chen, K. Persson, R. Kostecki and W. Yang, *Adv. Mater. Interfaces*, 2014, **1**, 1300115.
40 A. Jain, S. P. Ong, G. Hautier, W. Chen, W. D. Richards, S. Dacek, S. Cholia, D. Gunter, D. Skinner and G. Ceder, *APL Mater.*, 2013, **1**, 011002.
41 K. A. Persson, B. Waldwick, P. Lazic and G. Ceder, *Phys. Rev. B: Condens. Matter Mater. Phys.*, 2012, **85**, 235438.
42 M. Huang, T. Liu, Y. Deng, G. Geng, Y. Shen, Y. Lin and C. Nan, *Solid State Ionics*, 2011, **203**, 41.
43 D. Boryta and A. Mass, *Ind. Eng. Chem. Process Des. Dev.*, 1971, **10**, 489.

